Exposed facets dictate microbial methylation potential of mercury sulfide nanoparticles

Li Tian
Nankai University
Wenyu Guan
Nankai University
Yunyun Ji
Nankai University
Xin He
Nankai University
Wei Chen
Nankai University
Pedro Alvarez
Rice University
Tong Zhang (zhangtong@nankai.edu.cn)
Nankai University https://orcid.org/0000-0002-8151-3697

Article

Keywords: Methylmercury Formation, Global Mercury Contamination, Nanoparticulate Metacinnabar, Mercury Bioavailability, Interfacial Process

Posted Date: December 4th, 2020

DOI: https://doi.org/10.21203/rs.3.rs-119394/v1

Exposed facets dictate microbial methylation potential of mercury sulfide nanoparticles

Li Tian[1], Wenyu Guan[1], Yunyun Ji[1], Xin He[1], Wei Chen[1], Pedro J. J. Alvarez[2], Tong Zhang[1] *

1. *College of Environmental Science and Engineering, Ministry of Education Key Laboratory of Pollution Processes and Environmental Criteria, Tianjin Key Laboratory of Environmental Remediation and Pollution Control, Nankai University, 38 Tongyan Rd., Tianjin 300350, China*
2. *Department of Civil and Environmental Engineering, Rice University, 6100 Main Street, Houston, TX 77005, USA*

* Corresponding author: zhangtong@nankai.edu.cn

Manuscript prepared for *Nature Geoscience*

Methylmercury formation is the major concern of global mercury contamination. Accurate prediction of methylmercury production remains elusive due in part to the lack of mechanistic understanding of microbial methylation potential of particulate-phase mercury. Here we show that the methylation potential of nanoparticulate metacinnabar, which is formed during the early stage of mercury mineralization and is ubiquitous in contaminated soils and sediments, is determined by its exposed facets. Nanoparticulate metacinnabar with higher (111) content exhibits significantly greater affinity to the methylating bacterium *Desulfovibrio desulfuricans* ND132, leading to higher methylmercury production. This is likely attributable to the favored binding between the (111) facet and the protein transporter responsible for mercury cellular uptake prior to methylation. The (111) facet of metacinnabar tends to diminish during nanocrystal growth, but natural ligands alleviate this process by preferentially adsorbing to the (111) facet (verified with adsorption experiments using facet-engineered model materials coupled with theoretical calculations). This facet evolution of metacinnabar and its subsequent effect on mercury bioavailability explain the intriguing observation that methylation potential of nanoparticulate mercury is surface-area-independent. Our discovery provides new mechanistic insights for interfacial processes involved in nanoparticle−microorganism interactions that have important implications for understanding the environmental behavior of mercury and other nutrient or toxic elements associated with widely present crystalline nanoparticles.

Methylmercury (MeHg) production is primarily mediated by anaerobic microorganisms in natural aquatic environment[1] and largely determined by the bioavailability of inorganic mercury to microbial methylators[2]. A variety of different mercury species, including elemental mercury[3,4], dissolved mercury complexes[5] and mercury sulfide (HgS) nanoparticles[6], have been demonstrated to be available for methylation. In recent years, a growing body of evidence has revealed that MeHg production cannot be accurately predicted by the aqueous speciation of mercury alone, pointing to the essential role of particulate phase in controlling mercury methylation[7-10]. In fact, nanoparticulate mercury has been detected in various environmental matrices, such as soils, marshes and estuarine and marine water and sediments, which are natural 'hotspots' of MeHg production and accumulation[11-15]. Due to the kinetically-hindered mineralization processes in the presence of the ubiquitous natural organic matter (NOM) and sulfide[16-18], mercury-containing nanoparticles are expected to be prevalent in anaerobic environments. Moreover, recently proposed biological and photochemical pathways of the formation of mercury sulfide nanoparticles have extended the known occurrence of nanoparticulate mercury to 'new' natural settings (e.g., non-sulfidic condition, oxygenated environment)[19-22]. Hence, elucidating the mechanisms of and factors affecting the microbial methylation potential of mercury sulfide nanoparticles is critical for establishing risk assessment models of mercury pollution and understanding global biogeochemical cycling of mercury.

It is well known that nanoparticles are widely present in all environmental compartments due to natural and anthropogenic processes, and that they often exhibit environmental behaviors that are different from their bulk-scale counterparts because of

unique physicochemical properties at the nano-scale[23-26]. Indeed, nanoparticulate metacinnabar (i.e., a crystalline phase of HgS) appears to be significantly more available for microbial methylation compared to the bulk-scale metacinnabar[6,8]; however, the methylation potential of this particulate mercury phase drastically decreases during aging while remaining as nanoparticles[6]. Here, we demonstrate that the aging-induced changes in the bioavailability of nanoparticulate mercury for methylation is independent of the surface area or size of the nanoparticles; rather, it is dictated by the exposed facet, an intrinsic property of crystalline nanoparticles that define nano-specific interfacial reactions.

Aging-induced decrease in methylation potential of HgS nanoparticles is independent of surface area. Mercury sulfide nanoparticles remained bioavailable for methylation during the entire aging period in this research (i.e., 0-21 days), and the methylation potential of nanoparticulate mercury was altered by aging in a manner independent of surface area (Fig. 1). Ionic mercury and sulfide were precipitated in the presence of naturally-occurring ligands that often co-exist with mercury in environmental matrices, including Suwannee River humic acid (SRHA), Suwannee River fulvic acid (SRFA), and glutathione (GSH), and the precipitation products were immediately formed and left to age in anaerobic water for up to 21 days. The dominant products were nanoparticulate metacinnabar with particle diameter of 4.8-7.4 nm. These nanoparticles appeared to be relatively stable in size, surface area and aggregation status during aging (Fig. 1e-f; Supplementary Fig. 1-3; Supplementary Table 1), which corroborates previous studies that demonstrated the persistent occurrence of nanoparticulate mercury in aquatic

environment[11-16,18,27].

After aging for different time periods, the HgS nanoparticles were exposed to sulfate reducing bacteria (i.e., *Desulfovibrio desulfuricans* ND132), a major microbial group that drives mercury methylation in the environment[1,28]. The total mercury addition and microbial growth were consistent among all treatments receiving HgS aged for different time periods (Supplementary Fig. 4-5). The control group of HgS that precipitated without ligands exhibited minimal methylation potential (Fig. 1a). MeHg production from HgS nanoparticles formed in the presence of natural ligands diminished as the aging period prolonged (Fig. 1b-d), which cannot be explained by the aging-induced changes in the geometric diameter, surface area, crystallite diameter, hydrodynamic diameter or zeta potential of the nanoparticles (Fig. 1e-f; Supplementary Table 1). For instance, during aging from 1 to 21 d, the methylation potential of SRHA−HgS and SRFA−HgS nanoparticles (i.e., nanoparticles formed from precipitation of HgS with SRHA or SRFA) decreased by 65.0% and 62.0%, respectively (Fig. 1b-c), whereas differences in the size, surface area and charge of these particles were statistically insignificant (Fig. 1e-f; Supplementary Table 1). In general, nanoparticles tend to be highly reactive because of the large specific surface area[23-26]. However, in the case of microbial methylation of nanoparticulate mercury, structural surface properties other than surface area determined the reactivity of these nanoparticles.

Methylation potential of HgS nanoparticles depends on exposed facets. The exposed crystal facets of nanoparticulate metacinnabar changed during aging and strongly influenced the bioavailability and methylation potential of HgS nanoparticles (Fig. 1;

Supplementary Fig. 4-6). The dominant exposed facet of HgS precipitated with or without natural ligands was the (111) facet of metacinnabar according to the corresponding characteristic peak on the X-ray diffraction (XRD) spectra (Supplementary Fig. 6) and the lattice spacing on the high-resolution transmission electron microscopy (HR-TEM) images (Supplementary Fig. 1-3). The relative intensity of the (111) peak versus (220) peak in the XRD spectra was used to estimate the relative content of these facets[29]. The relative content of the (111) facet of metacinnabar generally decreased during aging (Fig. 1g), indicating a fast crystal growth along this dominant facet[30]. More importantly, this trend of changing exposed facets coincides with the trend of reducing methylation potential of HgS during aging (Fig. 1a-d), which underscores the potential role of the (111) facet in supplying bioavailable mercury for methylation. When mercury sulfide was co-precipitated with natural ligands, SRHA, SRFA and GSH, a markedly larger content of metacinnabar (111) facet was detected from the precipitation products (i.e., HgS nanoparticles), particularly during the early stage of mineralization (0-1 day), relative to the HgS precipitated without ligands (Fig. 1g). These results may, at least partially, explain the promoting effect of NOM and low-molecular-weight thiol ligands on mercury methylation reported in previous field and laboratory investigations[9,31,32].

To further discern the role of exposed facet in modulating microbial methylation of nanoparticulate mercury, two model materials of metacinnabar with relatively high (111) content (model material I) and low (111) content (model material II) were synthesized and examined in microbial methylation experiments (Supplementary Fig. 7-8; Supplementary Table 2). These model materials were synthesized to be nano-scale particles that exhibited similar size and morphology (Supplementary Fig. 7;

Supplementary Table 2). After incubation with the methylating bacteria *D. desulfuricans* ND132, MeHg production from material I was significantly greater compared with material II, while the total mercury concentrations and cell numbers were rather similar in all test cultures (Supplementary Fig. 8). Taken together, our results reveal that nano-scale metacinnabar that occurs during the early mercury mineralization stage likely represents the bioavailable particulate-phase precursors for MeHg production, and the exposed facet is a crucial parameter for determining the methylation potential of nano-metacinnabar.

Bacterial association with HgS nanoparticles depends on exposed facets. Our previous research on microbial methylation of HgS nanoparticles presumed the potential correlation between MeHg production and the release of dissolved mercury species (<20 nm) from particulate phase, which explained the variation in the bioavailability of nanoparticulate versus bulk-particulate mercury[6]. Nevertheless, recent mercury methylation studies revealed that bioavailability of particulate mercury cannot be accurately assessed by its leaching potential of inorganic mercury species into bulk solution[8,33]. In fact, bacteria−mineral association has been shown to be important for bio-transformation of goethite nanoparticles[34], and inorganic mercury appeared to strongly associate with bacterial cells through thiol-containing ligands[3,35,36], which apparently influenced the subsequent cellular uptake and methylation of mercury[10,37,38]. In this study, aging remarkably decreased the binding affinity and subsequent availability of nano-HgS for methylating bacteria, likely through altering the exposed facets of metacinnabar nanoparticles (Fig. 2-3).

We first conducted transmission electron microscopy coupled with energy dispersive spectroscopy (TEM−EDX) analysis of the thin sections of *D. desulfuricans* ND132 after nano-HgS exposure, and observed that metacinnabar nanoparticles formed with natural ligands and aged for different time periods were all abundantly associated with bacterial cells (Fig. 2; Supplementary Fig. 9). TEM images illustrated that nano-HgS attached to the inner and outer membranes as well as penetrated into the periplasm and cytosol, with the total number of cell-associated nanoparticles substantially decreasing upon aging from 1 to 21 d (Fig. 2; Supplementary Fig. 9). Facet-engineered model materials were used to connect this aging-reduced cell association with the exposed facets of metacinnabar. After separating the cell-bound nanoparticles from the freely suspended nanoparticles using density gradient centrifugation, the extent of nanoparticle−cell binding was quantified and appeared to be significantly larger in the treatment of model material I versus II (Supplementary Fig. 8b). These data suggest that nanoparticle−cell association is facet-dependent and that the (111) facet of metacinnabar has the highest affinity to the methylating bacteria.

Multiple lines of evidence have pointed to the essential role of periplasmic divalent metal transporters in dictating cellular transport of inorganic mercury across the bacterial cell membrane before intracellular methylation[38-43]. Here we show that addition of divalent zinc, Zn(II), to cultures of *D. desulfuricans* ND132 considerably inhibited microbial methylation of nano-HgS (Fig. 3a; Supplementary Fig. 10). This suggests the relevance of the zinc transport system of *D. desulfuricans* ND132 to investigate the facet-dependent binding and intracellular transport of nanoparticulate metacinnabar. Accordingly, binding between different exposed facets of nanoparticulate metacinnabar

and a periplasmic substrate-binding protein of the zinc transport system of *D. desulfuricans* ND132, ZnuA[44], was assessed using molecular dynamics simulations (Fig. 3b-k). Compared with the (220) and (311) facets, the (111) facet associated more sufficiently with ZnuA, as indicated by the larger facet−protein contact atom number and contact surface area (Fig. 3b-f). Within 1-nm interfacial distance, a greater number of amino acid residues bound to the (111) facet than the other facets, and both van der Waals force and electrostatic interaction (measured via the Van der Waals energy and Coulomb energy of the facet−protein systems) contributed to the facet-dependent transporter binding (Fig. 3g-k). The favored binding of metacinnabar (111) facet with metal transporters likely initiates uptake and methylation of mercury, which makes this facet relatively bioavailable.

Aging-induced diminishing of bioavailable facet of HgS nanoparticles is alleviated by facet-dependent preferential adsorption to natural ligands. The (111) facet of metacinnabar that actively participated in microbial methylation was preserved during mineralization, due to its preferential adsorption to natural ligands (Fig. 4). It is worth noting that fast crystal growth along certain direction often results in shrinking or elimination of the corresponding facet, which may be stabilized via adsorption of surface modifiers to reduce surface energy[30,45,46]. During the early stage of HgS mineralization, three main facets, including (111), (220) and (311) of metacinnabar were immediately formed, while the (111) facet exhibited preferential adsorption with natural ligands, according to the experimental data of ligand adsorption onto facet-engineered model materials complemented with theoretical calculations using density functional theory

(Fig. 4). The adsorbed amount of SRHA, SRFA and GSH on model material I was consistently greater than that on model materials II and the difference appeared to be 2- to 3-fold at the end of the adsorption experiments (Fig. 4a-c).

The favorable adsorption process on the (111) facet was also supported by the lower adsorption energy and larger density of active binding sites of the (111) facet toward GSH, compared to the (220) and (311) facets (Fig. 4d-g). Particularly, all mercury on the (111) facet are unsaturated three-coordinated atoms, which are prone to forming inner-sphere coordination bonds and inducing chemical adsorption of ligand-rich compounds (as indicated by the apparently negative adsorption energy, -1.33 eV). Indeed, both Hg $4f_{7/2}$ and Hg $4f_{5/2}$ peaks on the X-ray photoelectron spectroscopy (XPS) spectra of nano-HgS that formed with natural ligands prominently shifted to lower values of binding energy relative to the standard XPS spectrum of metacinnabar (Supplementary Fig. 11). These data confirm that the natural ligands strongly interacted with surficial mercury atoms of nanoparticulate metacinnabar via inner-sphere coordination. This chemical binding remained relatively stable during aging, as the binding energies of the mercury peaks were consistent among 1-d, 11-d and 21-d aged nano-HgS samples (Supplementary Fig. 11). The facet-dependent ligand adsorption not only explains the 'protecting effect' of natural ligands on the (111) facet of metacinnabar during HgS mineralization (Fig. 1g), but is also in line with the role of ligand-rich molecules (e.g., protein, peptide, surfactant, NOM) in modulating the crystalline faces of a diverse variety of pathological, engineered and naturally-occurring minerals[30,45,47,48].

Implications for metal biogeochemistry. Even though the 'new' mercury input may

only represent a small mercury fraction from a mass balance standpoint, it is the predominant source of MeHg that causes the environmental risks. Moreover, the vast majority of legacy mercury is susceptible to local and global scale perturbations, and can be 'renewed' by natural or anthropogenic processes (Fig. 5), such as global climate change, site remediation and altered landscape utilization[49-51]. In previous field studies, the methylation potential of the 'newly' deposited mercury appeared to be 1.5-2.8 times greater than that of the native mercury pool[52,53]. Similar magnitude of the aging-induced decreases in methylation potential was observed in our research on nanoparticulate mercury; i.e., newly formed nano-HgS was 1.6-4.9 times more available for microbial methylation than the aged nano-HgS during a 21-d time period, even though metacinnabar persistently remained at nano-scale. Considering that nanoparticulate mercury takes up a major fraction (12-93%) of the total mercury pool in natural aquatic systems[14,15], our research offers a mechanistic understanding of the dynamic changes in the methylation potential of the 'new' mercury inputs, and has paved the way toward incorporating particulate phases and interfacial processes into predictive models of MeHg production (Fig. 5). This knowledge is needed for assessing the time scales of biogeochemical processes leading to MeHg accumulation and subsequently informing remedial practice and management of mercury-impacted ecosystems with response time.

Preferential binding between ligand-rich molecules with fast-formed crystal faces may be nature's tool for tailoring the crystal structure and tuning the bioavailability of reactive mineral phases. The ligand-modulated facet evolution of nanoparticles during mineralization should not be limited to mercury sulfide and could be extended to the prevalent occurrence of nanominerals containing nutrient (e.g., Fe, Mn, Zn, Cu) or toxic

elements (e.g., Cd, Pb). These nanominerals likely represent the particulate phase that remains bioavailable for a widely variable time period and play vital roles in the biogeochemical cycling of the corresponding elements, leading to beneficial or detrimental environmental consequences. Hence, it is of utmost environmental significance to identify bioavailable mineral surfaces and understand structure-property relationships for bioavailability. Such interactions at mineral surfaces are particularly relevant for shaping the microbial ecology of mineral-dwelling communities[54,55] that substantially contribute to the earth's energy and biomass production (e.g., chemosynthesis driven by metal sulfides[56] and extracellular electron transfer driven by metal oxides[57,58]), as well as the biogeochemical cycles of essential elements (e.g., C and N)[59].

Acknowledgements

This research was supported by the National Key Research and Development Program of China (2018YFC1800705, 2019YFC1804400), the National Natural Science Foundation of China (Grants 21976095, 41603099), and the Ministry of Education of China (T2017002). Partial support for PA was provided by the NSF Nanosystems Engineering Research Center for Nanotechnology-Enabled Water Treatment (ERC-1449500). We thank Cynthia C. Gilmour for supplying the strain of *D. desulfuricans* ND132, and Heileen Hsu-Kim and Hui Henry Teng for helpful discussion regarding manuscript preparation.

Author contributions

L.T. and W.G. carried out the experiments and data analysis. T.Z. conceived the study and supervised the research. All authors contributed intellectual input to this study and drafted the manuscript.

Competing interests

The authors declare no competing interests.

References

1 Parks, J. M. et al. The genetic basis for bacterial mercury methylation. *Science* **339,** 1332-1335 (2013).

2 Hsu-Kim, H., Kucharzyk, K. H., Zhang, T. & Deshusses, M. A. Mechanisms regulating mercury bioavailability for methylating microorganisms in the aquatic environment: a critical review. *Environ. Sci. Technol.* **47,** 2441-2456 (2013).

3 Colombo, M. J., Ha, J. Y., Reinfelder, J. R., Barkay, T. & Yee, N. Anaerobic oxidation of Hg(0) and methylmercury formation by *Desulfovibrio desulfuricans* ND132. *Geochim. Cosmochim. Acta* **112,** 166-177 (2013).

4 Hu, H. Y. et al. Oxidation and methylation of dissolved elemental mercury by anaerobic bacteria. *Nat. Geosci.* **6,** 751-754 (2013).

5 Benoit, J. M., Gilmour, C. C., Mason, R. P. & Heyes, A. Sulfide controls on mercury speciation and bioavailability to methylating bacteria in sediment pore waters. *Environ. Sci. Technol.* **33,** 951-957 (1999).

6 Zhang, T. et al. Methylation of mercury by bacteria exposed to dissolved, nanoparticulate, and microparticulate mercuric sulfides. *Environ. Sci. Technol.* **46,** 6950-6958 (2012).

7 Jonsson, S. et al. Mercury methylation rates for geochemically relevant Hg^{II} species in sediments. *Environ. Sci. Technol.* **46,** 11653-11659 (2012).

8 Zhang, T., Kucharzyk, K. H., Kim, B., Deshusses, M. A. & Hsu-Kim, H. Net methylation of mercury in estuarine sediment microcosms amended with dissolved, nanoparticulate, and microparticulate mercuric sulfides. *Environ. Sci. Technol.* **48,** 9133-9141 (2014).

9 Mazrui, N. M., Jonsson, S., Thota, S., Zhao, J. & Mason, R. P. Enhanced availability of mercury bound to dissolved organic matter for methylation in marine sediments. *Geochim. Cosmochim. Acta* **194,** 153-162 (2016).

10 Zhang, L. J. et al. Mercury sorption and desorption on organo-mineral particulates as a source for microbial methylation. *Environ. Sci. Technol.* **53,** 2426-2433 (2019).

11 Barnett, M. O. et al. Formation of mercuric sulfide in soil. *Environ. Sci. Technol.* **31,** 3037-3043 (1997).

12 Patty, C. et al. Using X-ray microscopy and Hg L_3 XAMES to study Hg binding in the rhizosphere of *Spartina* cordgrass. *Environ. Sci. Technol.* **43,** 7397-7402 (2009).

13 Gilmour, C. et al. Distribution and biogeochemical controls on net methylmercury production in Penobscot River marshes and sediment. *Sci. Total Environ.* **640,** 555-569 (2018).

14 Stordal, M. C., Gill, G. A., Wen, L. S. & Santschi, P. H. Mercury phase speciation in the surface waters of three Texas estuaries: importance of colloidal forms. *Limnol. Oceanogr.* **41,** 52-61 (1996).

15 Guentzel, J. L., Powell, R. T., Landing, W. M. & Mason, R. P. Mercury associated with colloidal material in an estuarine and an open-ocean environment. *Mar. Chem.* **55,** 177-188 (1996).

16 Deonarine, A. & Hsu-Kim, H. Precipitation of mercuric sulfide nanoparticles in NOM-containing water: implications for the natural environment. *Environ. Sci. Technol.* **43,** 2368-2373 (2009).

17 Poulin, B. A. et al. Effects of sulfide concentration and dissolved organic matter characteristics on the structure of nanocolloidal metacinnabar. *Environ. Sci. Technol.* **51,** 13133-13142 (2017).

18 Mazrui, N. M. et al. The precipitation, growth and stability of mercury sulfide nanoparticles formed in the presence of marine dissolved organic matter. *Environ. Sci. Proc. Impacts* **20,** 642-656 (2018).

19 Manceau, A., Wang, J., Rovezzi, M., Glatzel, P. & Feng, X. Biogenesis of mercury–sulfur nanoparticles in plant leaves from atmospheric gaseous mercury. *Environ. Sci. Technol.* **52,** 3935-3948 (2018).

20 Manceau, A. et al. Formation of mercury sulfide from Hg(II)-thiolate complexes in natural organic matter. *Environ. Sci. Technol.* **49,** 9787-9796 (2015).

21 Luo, H. W. et al. Photochemical reactions between mercury (Hg) and dissolved organic matter decrease Hg bioavailability and methylation. *Environ. Pollut.* **220,** 1359-1365 (2017).

22 Thomas, S. A., Rodby, K. E., Roth, E. W., Wu, J. S. & Gaillard, J. F. Spectroscopic and microscopic evidence of biomediated HgS species formation from Hg(II)-cysteine complexes: implications for Hg(II) bioavailability. *Environ. Sci. Technol.* **52,** 10030-10039 (2018).

23 Hochella, M. F. et al. Nanominerals, mineral nanoparticles, and earth systems. *Science* **319,** 1631-1635 (2008).

24 Wang, Y. F. Nanogeochemistry: nanostructures, emergent properties and their control on geochemical reactions and mass transfers. *Chem. Geol.* **378,** 1-23 (2014).

25 Sharma, V. K., Filip, J., Zboril, R. & Varma, R. S. Natural inorganic nanoparticles-formation, fate, and toxicity in the environment. *Chem. Soc. Rev.* **44,** 8410-8423 (2015).

26 Hochella, M. F. et al. Natural, incidental, and engineered nanomaterials and their impacts on the earth system. *Science* **363,** 1414-1424 (2019).

27 Lowry, G. V., Shaw, S., Kim, C. S., Rytuba, J. J. & Brown, G. E. Macroscopic and microscopic observations of particle-facilitated mercury transport from New Idria and sulphur bank mercury mine tailings. *Environ. Sci. Technol.* **38,** 5101-5111 (2004).

28 Gilmour, C. C. et al. Sulfate-reducing bacterium *Desulfovibrio desulfuricans* ND132 as a model for understanding bacterial mercury methylation. *Appl. Environ. Microbiol.* **77,** 3938-3951 (2011).

29 Liu, L. et al. Facet energy and reactivity versus cytotoxicity: the surprising behavior of CdS nanorods. *Nano Lett.* **16,** 688-694 (2016).

30 Jun, Y. W. et al. Surfactant-assisted elimination of a high energy facet as a means of controlling the shapes of TiO_2 nanocrystals. *J. Am. Chem. Soc.* **125,** 15981-15985 (2003).

31 Graham, A. M., Aiken, G. R. & Gilmour, C. C. Effect of dissolved organic matter source and character on microbial Hg methylation in Hg-S-DOM solutions. *Environ. Sci. Technol.* **47,** 5746-5754 (2013).

32 Bouchet, S. et al. Linking microbial activities and low-molecular-weight thiols to Hg methylation in biofilms and periphyton from high-altitude tropical lakes in the Bolivian Altiplano. *Environ. Sci. Technol.* **52,** 9758-9767 (2018).

33 Rivera, N. A., Bippus, P. M. & Hsu-Kim, H. Relative reactivity and bioavailability of mercury sorbed to or coprecipitated with aged iron sulfides. *Environ. Sci. Technol.* **53,** 7391-7399 (2019).

34 Lower, S. K., Hochella, M. F. & Beveridge, T. J. Bacterial recognition of mineral surfaces: nanoscale interactions between *Shewanella* and α-FeOOH. *Science* **292,** 1360-1363 (2001).

35 Pedrero, Z. et al. Transformation, localization, and biomolecular binding of Hg species at subcellular level in methylating and nonmethylating sulfate-reducing bacteria. *Environ. Sci. Technol.* **46,** 11744-11751 (2012).

36 Dunham-Cheatham, S., Mishra, B., Myneni, S. & Fein, J. B. The effect of natural organic matter on the adsorption of mercury to bacterial cells. *Geochim. Cosmochim. Acta* **150,** 1-10 (2015).

37 Zhao, L. D. et al. Contrasting effects of dissolved organic matter on mercury methylation by *Geobacter sulfurreducens* PCA and *Desulfovibrio desulfuricans* ND132. *Environ. Sci. Technol.* **51,** 10468-10475 (2017).

38 Schaefer, J. K., Szczuka, A. & Morel, F. M. M. Effect of divalent metals on Hg(II) uptake and methylation by bacteria. *Environ. Sci. Technol.* **48,** 3007-3013 (2014).

39 Qian, C. et al. Quantitative proteomic analysis of biological processes and responses of the bacterium *Desulfovibrio desulfuricans* ND132 upon deletion of its mercury methylation genes. *Proteomics* **18,** 1700479 (2018).

40 Schaefer, J. K. et al. Active transport, substrate specificity, and methylation of Hg(II) in anaerobic bacteria. *Proc. Natl Acad. Sci. USA* **108,** 8714-8719 (2011).

41 Thomas, S. A., Mishra, B. & Myneni, S. C. B. Cellular mercury coordination environment, and not cell surface ligands, influence bacterial methylmercury production. *Environ. Sci. Technol.* **54,** 3960-3968 (2020).

42 Lin, H., Morrell-Falvey, J. L., Rao, B., Liang, L. & Gu, B. Coupled mercury–cell sorption, reduction, and oxidation on methylmercury production by *Geobacter sulfurreducens* PCA. *Environ. Sci. Technol.* **48,** 11969-11976 (2014).

43 Lu, X. et al. Nanomolar copper enhances mercury methylation by *Desulfovibrio desulfuricans* ND132. *Environ. Sci. Technol. Lett.* **5,** 372-376 (2018).

44 Brown, S. D. et al. Genome sequence of the mercury-methylating strain *Desulfovibrio desulfuricans* ND132. *J. Bacteriol.* **193,** 2078-2079 (2011).

45 Strehlau, J. H., Stemig, M. S., Penn, R. L. & Arnold, W. A. Facet-dependent oxidative goethite growth as a function of aqueous solution conditions. *Environ. Sci. Technol.* **50,** 10406-10412 (2016).

46 Guo, S. W., Ward, M. D. & Wesson, J. A. Direct visualization of calcium oxalate monohydrate crystallization and dissolution with atomic force microscopy and the role of polymeric additives. *Langmuir* **18,** 4284-4291 (2002).

47 Qiu, S. R. et al. Molecular modulation of calcium oxalate crystallization by osteopontin and citrate. *Proc. Natl Acad. Sci. USA* **101,** 1811-1815 (2004).

48 De Yoreo, J. J. & Dove, P. M. Shaping crystals with biomolecules. *Science* **306,** 1301-1302 (2004).

49 Hsu-Kim, H. et al. Challenges and opportunities for managing aquatic mercury pollution in altered landscapes. *Ambio* **47,** 141-169 (2018).

50 Obrist, D. et al. A review of global environmental mercury processes in response to human and natural perturbations: changes of emissions, climate, and land use. *Ambio* **47,** 116-140 (2018).

51 Schaefer, K. et al. Potential impacts of mercury released from thawing permafrost. *Nat. Commun.* **11,** 4650 (2020).

52 Hintelmann, H. et al. Reactivity and mobility of new and old mercury deposition in a Boreal forest ecosystem during the first year of the METAALICUS study. *Environ. Sci. Technol.* **36,** 5034-5040 (2002).

53 Meng, B. et al. The process of methylmercury accumulation in rice (*Oryza sativa* L.). *Environ. Sci. Technol.* **45,** 2711-2717 (2011).

54 Flemming, H.-C. & Wuertz, S. Bacteria and archaea on earth and their abundance in biofilms. *Nat. Rev. Microbiol.* **17,** 247-260 (2019).

55 Brewer, T. E. & Fierer, N. Tales from the tomb: the microbial ecology of exposed rock surfaces. *Environ. Microbiol.* **20,** 958-970 (2018).

56 Russell, M. J. & Hall, A. J. The emergence of life from iron monosulphide bubbles at a submarine hydrothermal redox and pH front. *J. Geol. Soc. London* **154,** 377-402 (1997).

57 Lovley, D. R. Dissimilatory Fe(III) and Mn(IV) reduction. *Microbiol. Rev.* **55,** 259-287 (1991).

58 Nealson, K. H. & Saffarini, D. Iron and manganese in anaerobic respiration: environmental significance, physiology, and regulation. *Annu. Rev. Microbiol.* **48,** 311-343 (1994).

59 Falkowski, P. G., Fenchel, T. & Delong, E. F. The microbial engines that drive earth's biogeochemical cycles. *Science* **320,** 1034-1039 (2008).

60 Birks, L. S. F., H. Particle size determination from X-ray line broadening. *J. Appl. Phys.* **17,** 687-691 (1946).

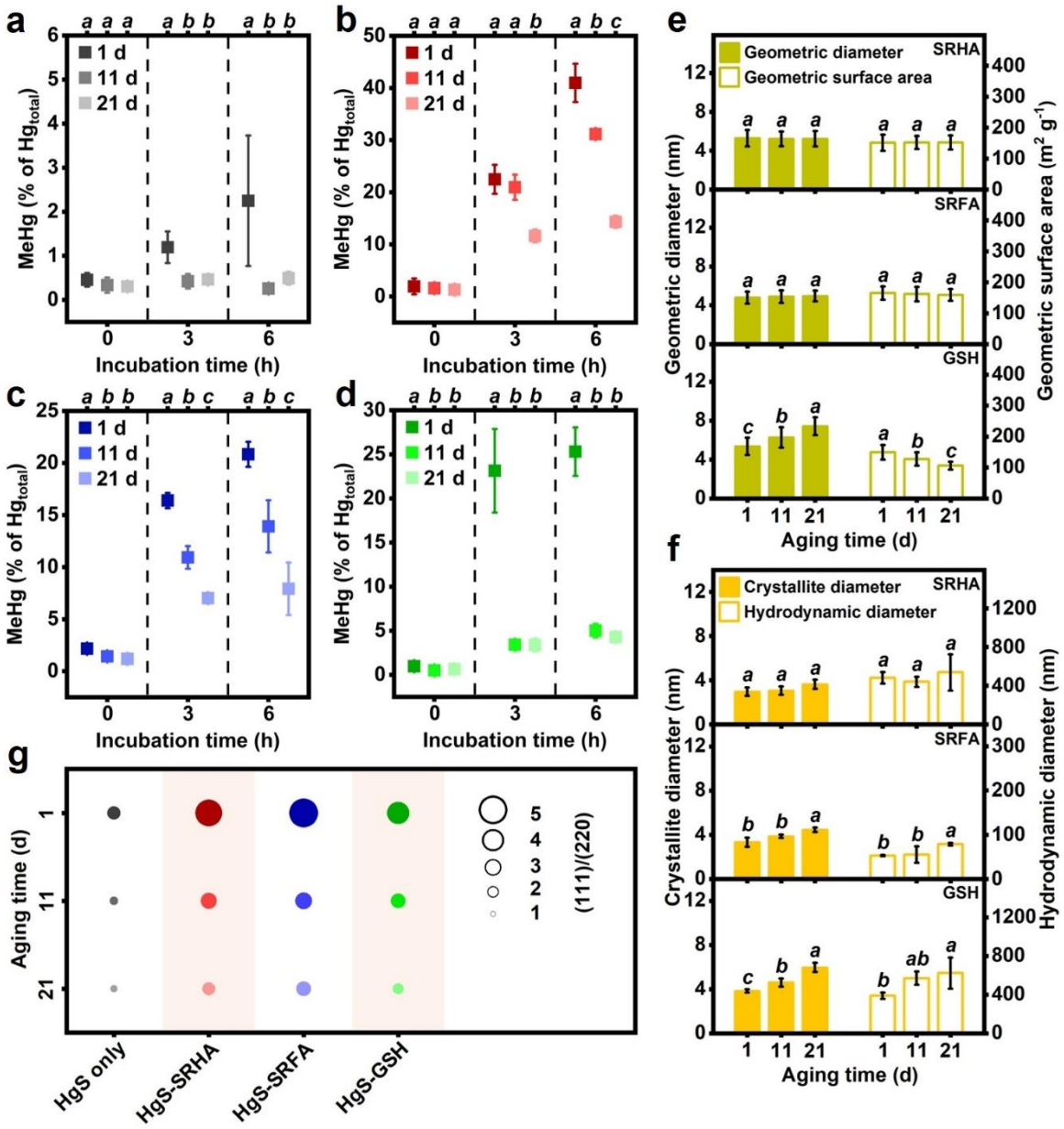
a
b
c
d
e
f
g
1 d
11 d
21 d
MeHg (% of Hg$_{total}$)
Incubation time (h)
Geometric diameter
Geometric surface area
SRHA
SRFA
GSH
Geometric diameter (nm)
Geometric surface area (m^2 g^{-1})
Aging time (d)
Crystallite diameter
Hydrodynamic diameter
Crystallite diameter (nm)
Hydrodynamic diameter (nm)
Aging time (d)
(111)/(220)
HgS only
HgS-SRHA
HgS-SRFA
HgS-GSH

Figure 1 Methylation potential and exposed facets of mercury sulfide nanoparticles, formed in the presence of natural ligands, significantly change during aging while particle size and surface area remain similar. a-d, Methylmercury (MeHg) production by *Desulfovibrio desulfuricans* ND132 normalized to the total mercury concentrations after exposure to 10 nM HgS formed in the absence of natural ligands (**a**) and HgS nanoparticles co-precipitated with Suwannee River humic acid (SRHA, **b**), Suwannee River fulvic acid (SRFA, **c**) or glutathione (GSH, **d**), and aged for 1 d, 11 d or 21 d. Values that are statistically different (p <0.05) among treatments with different aging time according to the one-way ANOVA are indicated by italic lowercase letters. Error bars represent ± 1 standard deviation (SD) of triplicate samples. **e,** The geometric diameters and geometric surface areas of HgS nanoparticles co-precipitated with SRHA, SRFA or GSH that aged for different time periods. Values that are statistically different (p <0.05) among treatments with different aging time according to the one-way ANOVA are indicated by italic lowercase letters. Error bars represent ± 1 SD of one hundred samples. **f,** The crystallite diameters and hydrodynamic diameters of HgS nanoparticles co-precipitated with SRHA, SRFA or GSH that aged for different time periods. The crystallite diameters were calculated according to the Scherrer formula[60] using the X-ray diffraction data (Supplementary Figure 6). Values that are statistically different (p <0.05) among treatments with different aging time according to the one-way ANOVA are indicated by italic lowercase letters. Error bars represent ± 1 SD of triplicate samples. **g,** Relative content of metacinnabar (111) facet in HgS formed in the presence or absence of natural ligands.

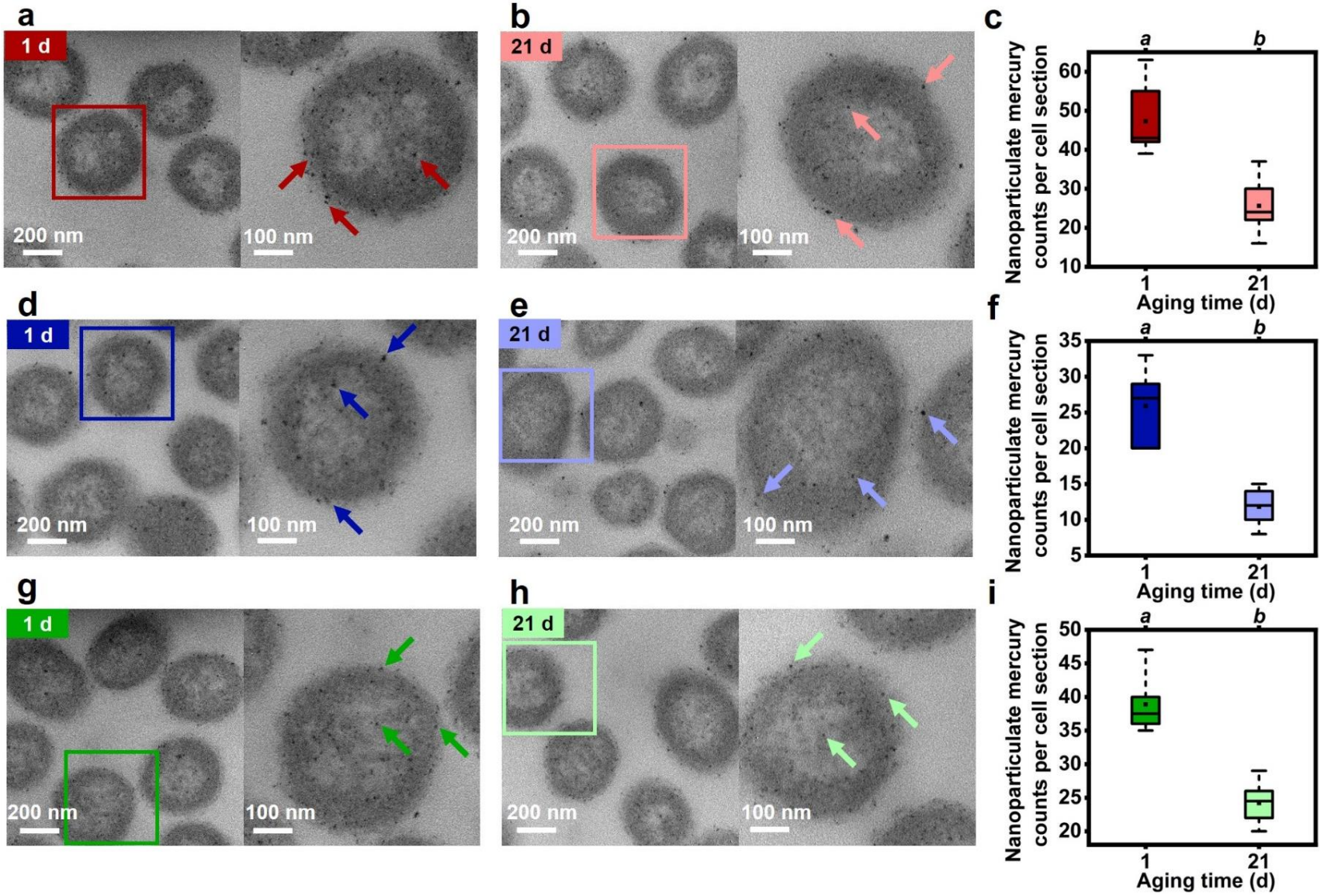
a
1 d
200 nm
100 nm
b
21 d
200 nm
100 nm
c
Nanoparticulate mercury counts per cell section
a
b
60
50
40
30
20
10
1
21
Aging time (d)
d
1 d
200 nm
100 nm
e
21 d
200 nm
100 nm
f
Nanoparticulate mercury counts per cell section
a
b
35
30
25
20
15
10
5
1
21
Aging time (d)
g
1 d
200 nm
100 nm
h
21 d
200 nm
100 nm
i
Nanoparticulate mercury counts per cell section
a
b
50
45
40
35
30
25
20
1
21
Aging time (d)

Figure 2 Association between methylating bacterial cells and mercury sulfide nanoparticles, formed in the presence of natural ligands, significantly decreases during aging. a,b,d,e,g,h, Transmission electron microscopy (TEM) images of *D. desulfuricans* ND132 after exposure to HgS nanoparticles co-precipitated with SRHA (**a,b**), SRFA (**d,e**), or GSH (**g,h**) and aged for 1 d (**a,d,g**) or 21 d (**b,e,h**). **c,f,i**, Nanoparticulate mercury counts per cell section of *D. desulfuricans* ND132 after exposure to HgS nanoparticles co-precipitated with SRHA (**c**), SRFA (**f**), or GSH (**i**). The bottom and top of the boxes show the first and third quartiles, respectively, the bar in the middle shows the median, the black solid dot shows the average value and the whiskers show the minimum and maximum values of ten replicate samples. Values that are statistically different (p <0.05) between treatments with different aging time according to the independent t-test are indicated by italic lowercase letters.

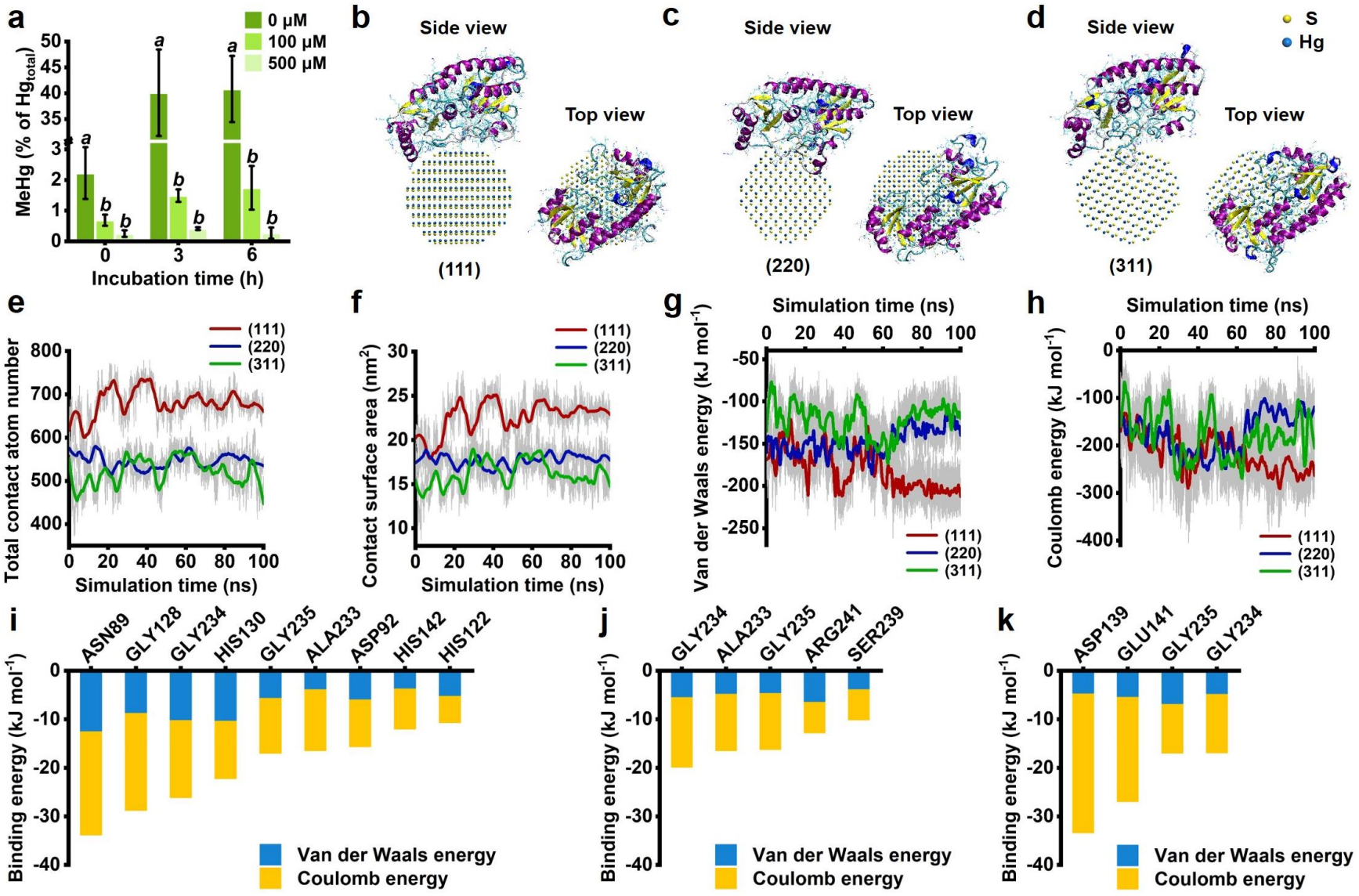
a
0 μM
100 μM
500 μM
MeHg (% of Hg$_{total}$)
Incubation time (h)
b
Side view
Top view
(111)
c
Side view
Top view
(220)
d
Side view
Top view
S
Hg
(311)
e
Total contact atom number
Simulation time (ns)
(111)
(220)
(311)
f
Contact surface area (nm^2)
Simulation time (ns)
g
Van der Waals energy (kJ mol^{-1})
Simulation time (ns)
h
Coulomb energy (kJ mol^{-1})
Simulation time (ns)
i
Binding energy (kJ mol^{-1})
ASN89
GLY128
GLY234
HIS130
GLY235
ALA233
ASP92
HIS142
HIS122
Van der Waals energy
Coulomb energy
j
Binding energy (kJ mol^{-1})
GLY234
ALA233
GLY235
ARG241
SER239
Van der Waals energy
Coulomb energy
k
Binding energy (kJ mol^{-1})
ASP139
GLU141
GLY235
GLY234
Van der Waals energy
Coulomb energy

Figure 3 The (111) facet of nanoparticulate metacinnabar exhibits higher affinity for the divalent metal transporter of *D. desulfuricans* ND132, relative to the other exposed facets. a, MeHg production by *D. desulfuricans* ND132 normalized to the total mercury concentrations after exposure to Zn(II) and 10 nM HgS nanoparticles co-precipitated with GSH and aged for 1 d. Values that are statistically different (p <0.05) among treatments with different concentrations of Zn(II) according to the one-way ANOVA are indicated by italic lowercase letters. Error bars represent ± 1 SD of triplicate samples. **b-d**, Binding conformation of periplasmic solute-binding protein of zinc transport system of *D. desulfuricans* ND132, ZnuA, on facets (111) (**b**), (220) (**c**) and (311) (**d**) at 100 ns of molecular dynamics (MD) simulations. **e**, Time-dependent total contact atom number of an individual ZnuA within 1 nm from different facets of metacinnabar during MD simulations. **f**, Time-dependent contact surface area of an individual ZnuA on different facets of metacinnabar during MD simulations. **g,h**, Time-dependent van der Waals energy (**g**) and Coulomb energy (**h**) of ZnuA on different facets of metacinnabar during MD simulations. **i-k**, Binding energy of key amino acid residues (binding energy >10 kJ/mol) associated with facets (111) (**i**), (220) (**j**) and (311) (**k**) within 1 nm at the last 5 ns of MD simulations.

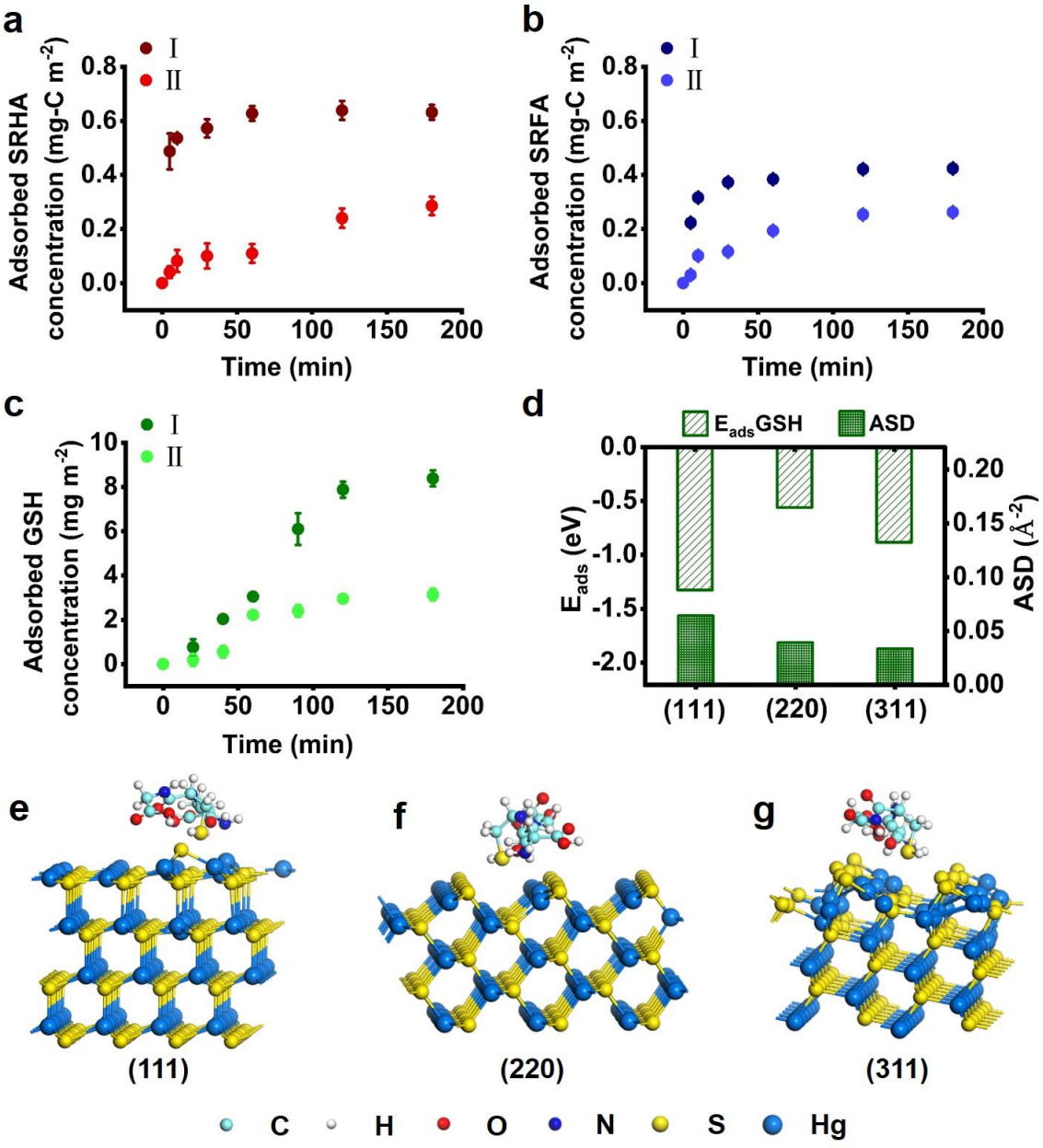

Figure 4 The (111) facet of nanoparticulate metacinnabar preferentially adsorbs with natural ligands. a-c, Adsorption of SRHA (**a**), SRFA (**b**) and GSH (**c**) to model HgS nanoparticle I *vs.* II. Error bars represent ± 1 SD of triplicate samples. **d,** Adsorption energy (E_{ads}) and active site density (ASD) of different crystal facets of metacinnabar adsorbed with GSH according to density function theory calculations. **e-g,** Three-dimensional views of GSH molecules adsorbed to facets (111) (**e**), (220) (**f**) and (311) (**g**) of metacinnabar.

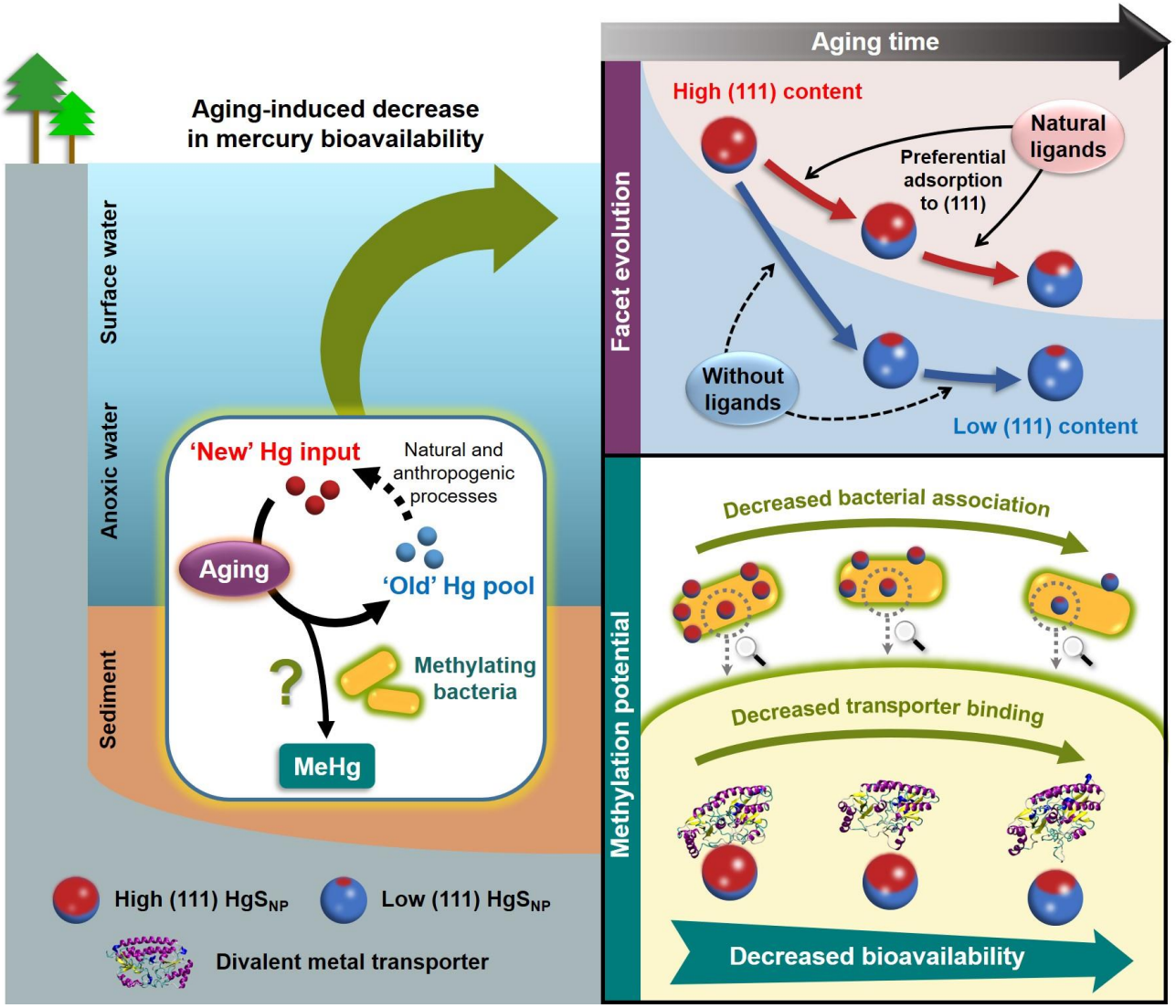
Aging-induced decrease
in mercury bioavailability
Surface water
Anoxic water
Sediment
'New' Hg input
Natural and
anthropogenic
processes
Aging
'Old' Hg pool
?
Methylating
bacteria
MeHg
High (111) HgS$_{NP}$
Low (111) HgS$_{NP}$
Divalent metal transporter
Aging time
Facet evolution
High (111) content
Natural
ligands
Preferential
adsorption
to (111)
Without
ligands
Low (111) content
Methylation potential
Decreased bacterial association
Decreased transporter binding
Decreased bioavailability

Figure 5 Conceptual illustration of aging-induced decrease in bioavailability and methylation potential of nanoparticulate metacinnabar due to facet evolution. The (111) facet of nanoparticulate metacinnabar decreases during aging and this process is mitigated by the preferential adsorption of natural ligands to (111), relative to the other exposed facets of metacinnabar. Nanoparticulate metacinnabar with large content of (111) facet strongly associate with divalent metal transporters of methylating bacteria, which enhances cellular uptake and methylation of nanoparticulate mercury. These findings explain the greater methylmercury production from the 'new' mercury input compared to the 'old' environmental mercury pool, which may be 'renewed' by various natural and anthropogenic processes.

Figures

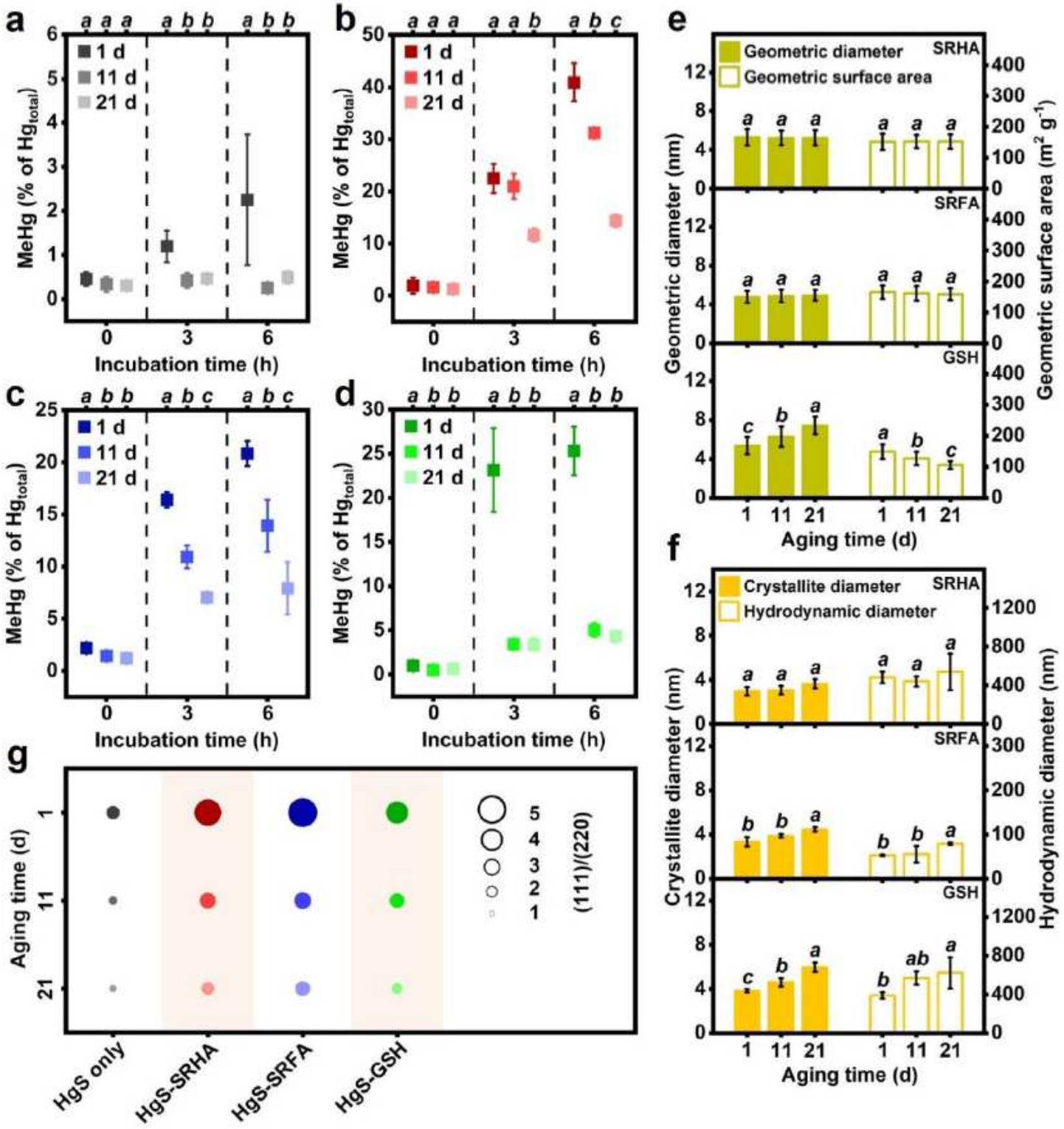

Figure 1

Methylation potential and exposed facets of mercury sulfide nanoparticles, formed in the presence of natural ligands, significantly change during aging while particle size and surface area remain similar. a-d, Methylmercury (MeHg) production by Desulfovibrio desulfuricans ND132 normalized to the total mercury

concentrations after exposure to 10 nM HgS formed in the absence of natural ligands (a) and HgS nanoparticles co-precipitated with Suwannee River humic acid (SRHA, b), Suwannee River fulvic acid (SRFA, c) or glutathione (GSH, d), and aged for 1 d, 11 d or 21 d. Values that are statistically different ($p < 0.05$) among treatments with different aging time according to the one-way ANOVA are indicated by italic lowercase letters. Error bars represent ± 1 standard deviation (SD) of triplicate samples. e, The geometric diameters and geometric surface areas of HgS nanoparticles co-precipitated with SRHA, SRFA or GSH that aged for different time periods. Values that are statistically different ($p < 0.05$) among treatments with different aging time according to the one-way ANOVA are indicated by italic lowercase letters. Error bars represent ± 1 SD of one hundred samples. f, The crystallite diameters and hydrodynamic diameters of HgS nanoparticles co-precipitated with SRHA, SRFA or GSH that aged for different time periods. The crystallite diameters were calculated according to the Scherrer formula60 using the X-ray diffraction data (Supplementary Figure 6). Values that are statistically different ($p < 0.05$) among treatments with different aging time according to the one-way ANOVA are indicated by italic lowercase letters. Error bars represent ± 1 SD of triplicate samples. g, Relative content of metacinnabar (111) facet in HgS formed in the presence or absence of natural ligands.

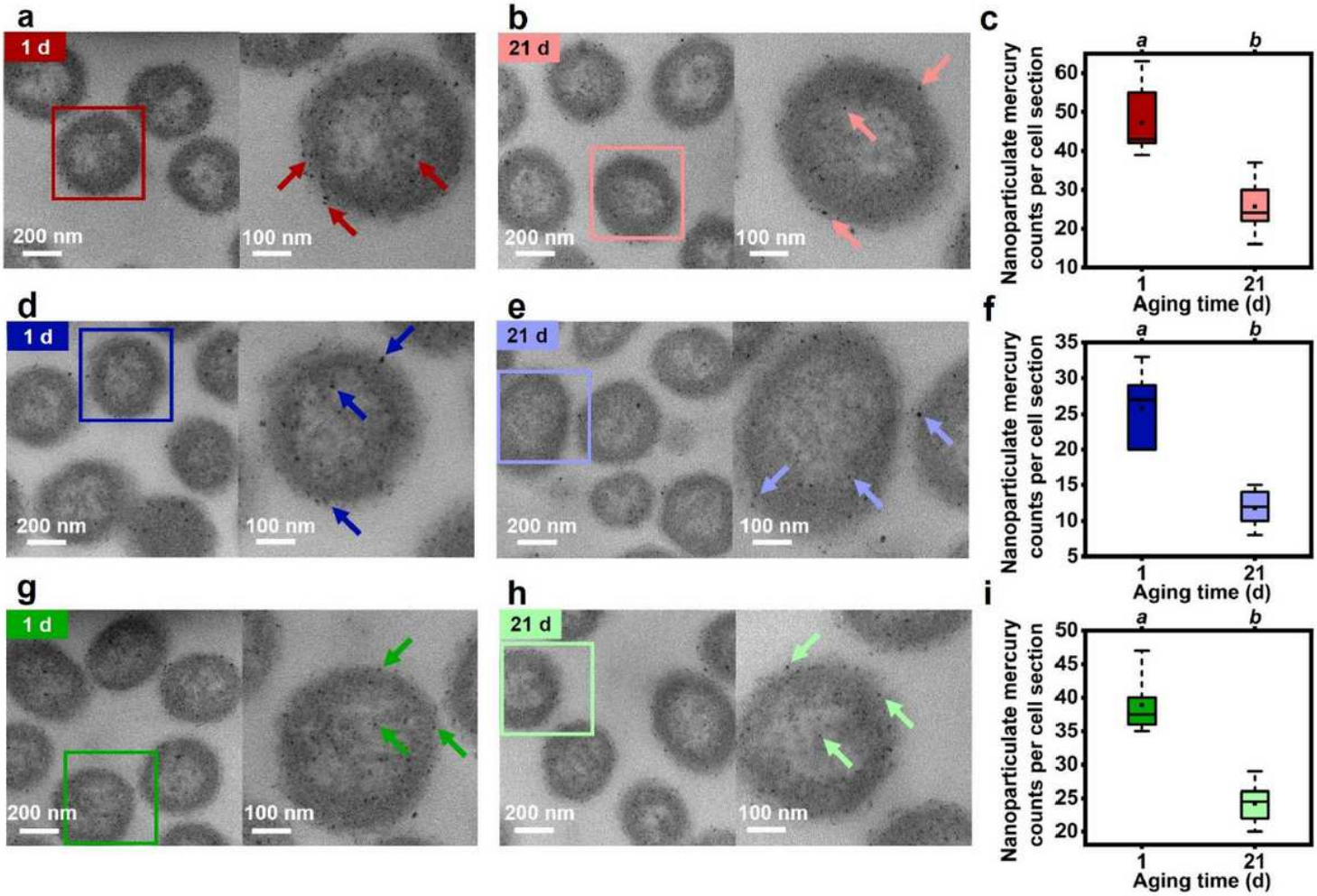

Figure 2

Association between methylating bacterial cells and mercury sulfide nanoparticles, formed in the presence of natural ligands, significantly decreases during aging. a,b,d,e,g,h, Transmission electron microscopy (TEM) images of D. desulfuricans ND132 after exposure to HgS nanoparticles co-precipitated with SRHA (a,b), SRFA (d,e), or GSH (g,h) and aged for 1 d (a,d,g) or 21 d (b,e,h). c,f,i, Nanoparticulate mercury counts per cell section of D. desulfuricans ND132 after exposure to HgS nanoparticles co-precipitated with SRHA (c), SRFA (f), or GSH (i). The bottom and top of the boxes show the first and third quartiles, respectively, the bar in the middle shows the median, the black solid dot shows the average value and the whiskers show the minimum and maximum values of ten replicate samples. Values that are statistically different ($p < 0.05$) between treatments with different aging time according to the independent t-test are indicated by italic lowercase letters.

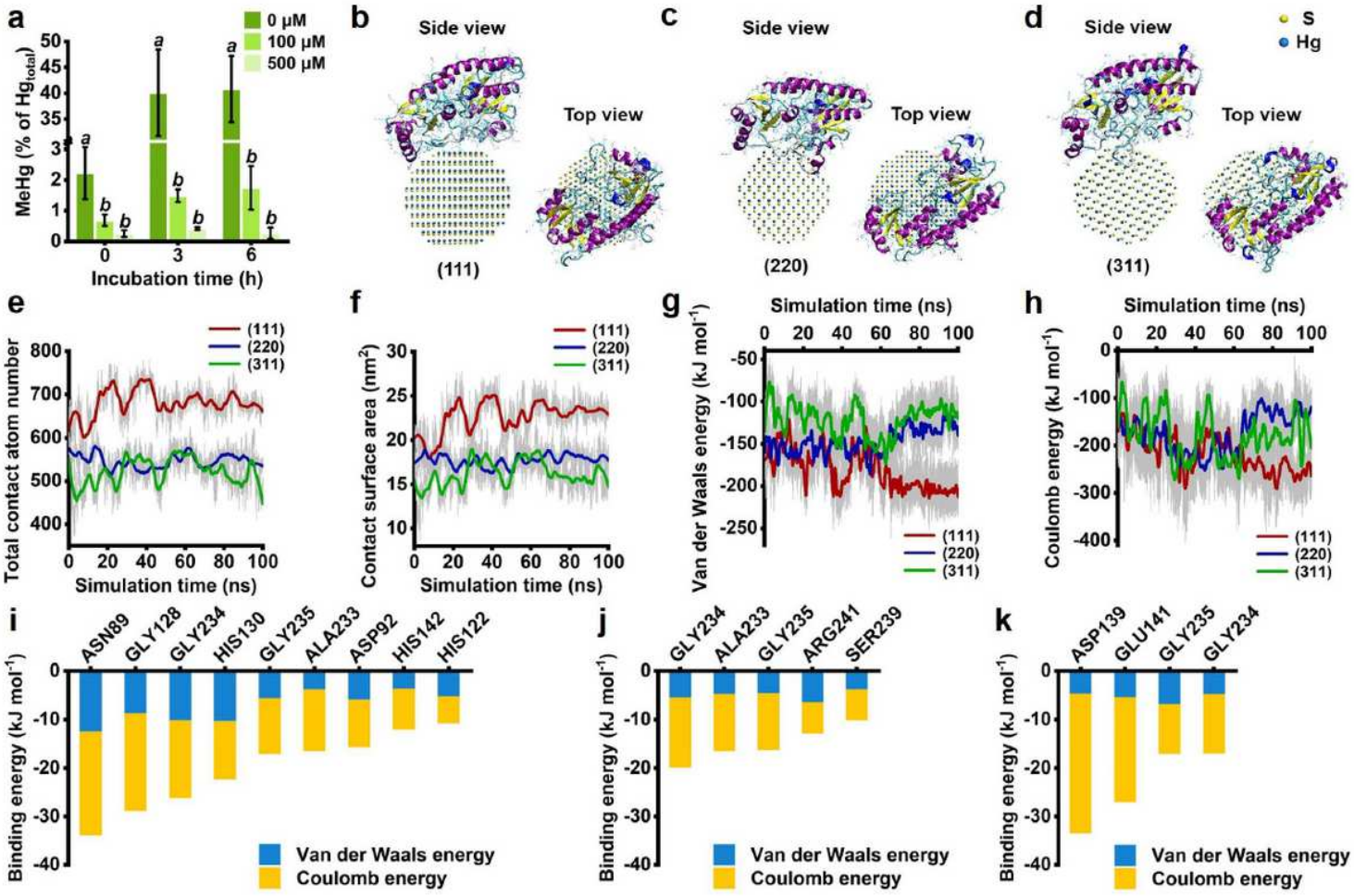

Figure 3

The (111) facet of nanoparticulate metacinnabar exhibits higher affinity for the divalent metal transporter of D. desulfuricans ND132, relative to the other exposed facets. a, MeHg production by D. desulfuricans ND132 normalized to the total mercury concentrations after exposure to Zn(II) and 10 nM HgS nanoparticles co-precipitated with GSH and aged for 1 d. Values that are statistically different ($p < 0.05$) among treatments with different concentrations of Zn(II) according to the one-way ANOVA are indicated by italic lowercase letters. Error bars represent ± 1 SD of triplicate samples. b-d, Binding conformation of periplasmic solute-binding protein of zinc transport system of D. desulfuricans ND132, ZnuA, on facets

(111) (b), (220) (c) and (311) (d) at 100 ns of molecular dynamics (MD) simulations. e, Time-dependent total contact atom number of an individual ZnuA within 1 nm from different facets of metacinnabar during MD simulations. f, Time-dependent contact surface area of an individual ZnuA on different facets of metacinnabar during MD simulations. g,h, Time-dependent van der Waals energy (g) and Coulomb energy (h) of ZnuA on different facets of metacinnabar during MD simulations. i-k, Binding energy of key amino acid residues (binding energy >10 kJ/mol) associated with facets (111) (i), (220) (j) and (311) (k) within 1 nm at the last 5 ns of MD simulations.

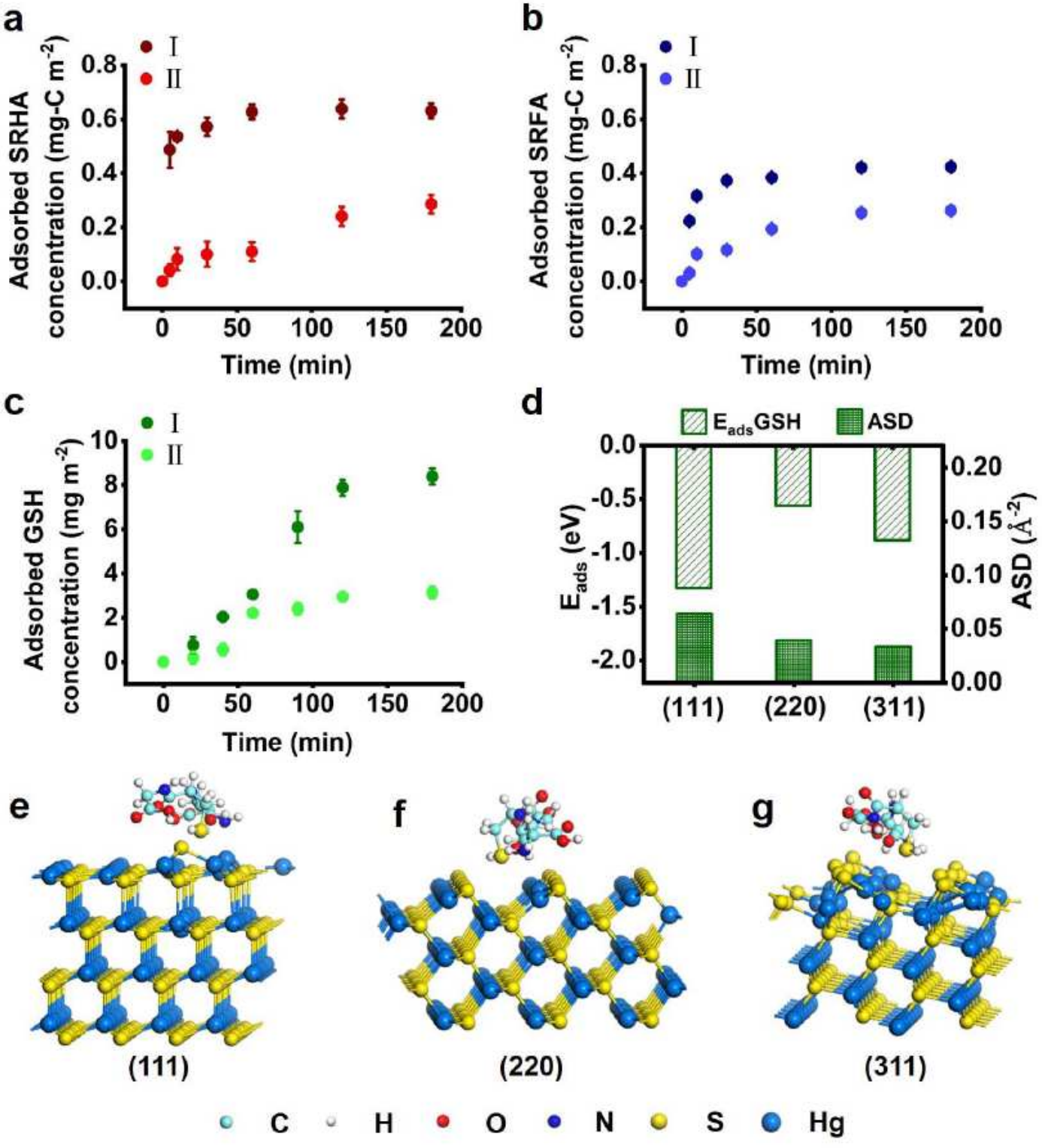

Figure 4

The (111) facet of nanoparticulate metacinnabar preferentially adsorbs with natural ligands. a-c, Adsorption of SRHA (a), SRFA (b) and GSH (c) to model HgS nanoparticle I vs. II. Error bars represent ± 1 SD of triplicate samples. d, Adsorption energy (Eads) and active site density (ASD) of different crystal facets of metacinnabar adsorbed with GSH according to density function theory calculations. e-g, Three-dimensional views of GSH molecules adsorbed to facets (111) (e), (220) (f) and (311) (g) of metacinnabar.

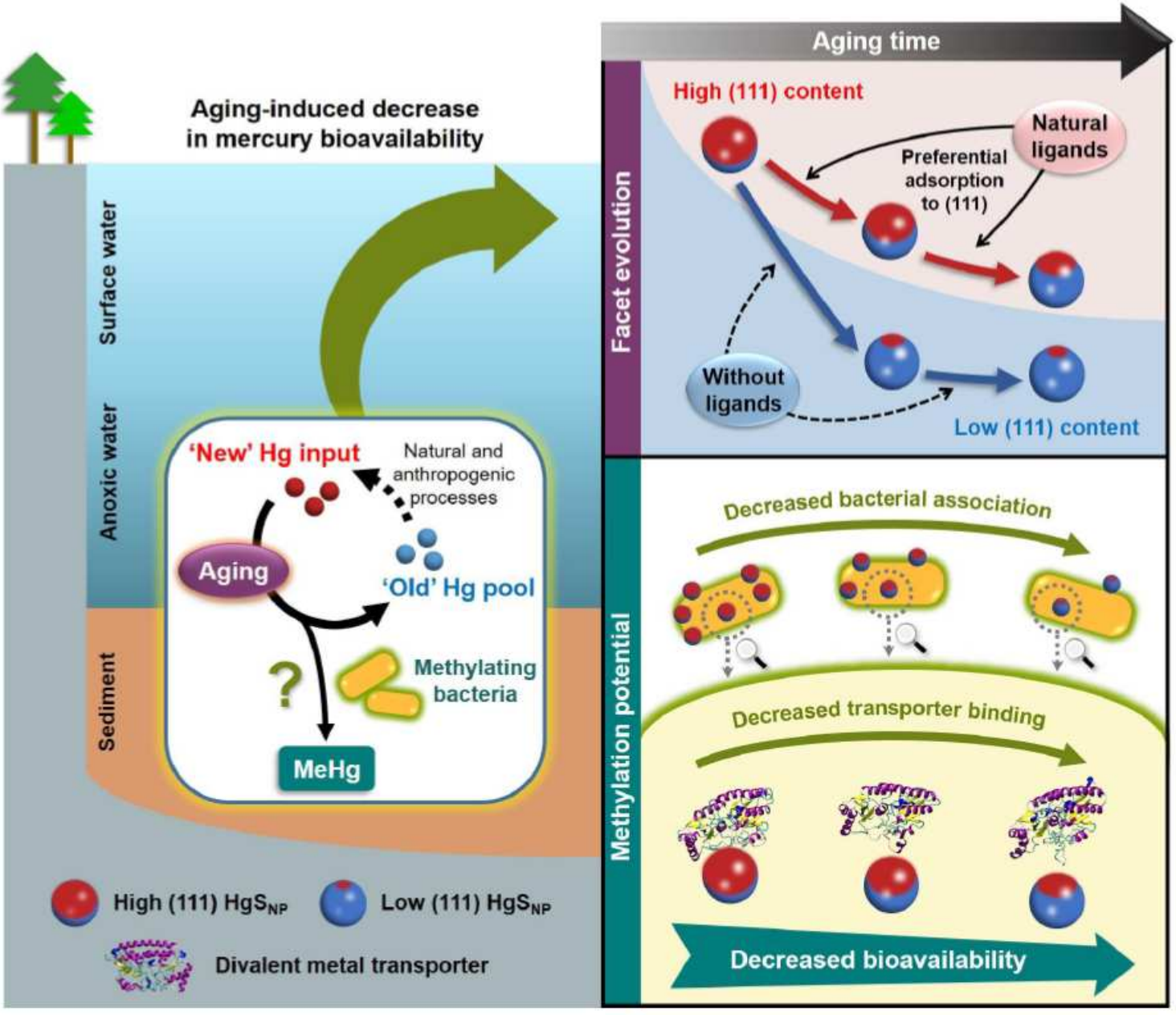

Figure 5

Conceptual illustration of aging-induced decrease in bioavailability and methylation potential of nanoparticulate metacinnabar due to facet evolution. The (111) facet of nanoparticulate metacinnabar decreases during aging and this process is mitigated by the preferential adsorption of natural ligands to

(111), relative to the other exposed facets of metacinnabar. Nanoparticulate metacinnabar with large content of (111) facet strongly associate with divalent metal transporters of methylating bacteria, which enhances cellular uptake and methylation of nanoparticulate mercury. These findings explain the greater methylmercury production from the ‘new’ mercury input compared to the ‘old’ environmental mercury pool, which may be ‘renewed’ by various natural and anthropogenic processes.

Supplementary Files

This is a list of supplementary files associated with this preprint. Click to download.

- SupportingInformationTianetalfinal.pdf